

Measuring the complex orbital angular momentum spectrum and spatial mode decomposition of structured light beams

ALESSIO D'ERRICO,¹ RAFFAELE D'AMELIO,¹ BRUNO PICCIRILLO,¹ FILIPPO CARDANO,^{1,*}  AND LORENZO MARRUCCI^{1,2}

¹Dipartimento di Fisica "Ettore Pancini", Università di Napoli Federico II, Complesso Universitario di Monte Sant'Angelo, Napoli, Italy

²CNR-ISASI, Institute of Applied Science and Intelligent Systems, Via Campi Flegrei 34, Pozzuoli (NA), Italy

*Corresponding author: filippo.cardano2@unina.it

Received 6 June 2017; revised 8 September 2017; accepted 20 September 2017 (Doc. ID 297496); published 27 October 2017

Light beams carrying orbital angular momentum are key resources in modern photonics. In many applications, the ability to measure the complex spectrum of structured light beams in terms of these fundamental modes is crucial. Here we propose and experimentally validate a simple method that achieves this goal by digital analysis of the interference pattern formed by the light beam and a reference field. Our approach allows one to also characterize the beam radial distribution, hence retrieving the entire information contained in the optical field. Setup simplicity and reduced number of measurements could make this approach practical and convenient for the characterization of structured light fields. © 2017 Optical Society of America

OCIS codes: (050.4865) Optical vortices; (260.6042) Singular optics; (230.6120) Spatial light modulators; (090.1970) Diffractive optics; (070.0070) Fourier optics and signal processing; (060.2605) Free-space optical communication.

<https://doi.org/10.1364/OPTICA.4.001350>

1. INTRODUCTION

In 1992, Allen *et al.* [1] showed that helical modes of light—paraxial beams featuring a helical phase factor $e^{im\phi}$, where ϕ is the azimuthal angle around the beam axis and m is an integer—carry a definite amount of orbital angular momentum (OAM) along the propagation axis, equal to $m\hbar$ per photon [2]. Important realizations of such optical modes include, for example, Laguerre–Gauss (LG) [1] and Hypergeometric Gaussian beams (HyGG) [3], which share the typical twisted wavefront but differ in their radial profiles. Controlled superpositions of helical modes, possibly combined with orthogonal polarization states via spin-orbit interaction [4,5], result in spatially structured beams that are proving useful for a broad set of photonic applications [6] such as classical and quantum optical communication [7–10], quantum information processing [11–13], and quantum simulations [14,15]. The ability to experimentally ascertain the OAM values associated with individual helical modes represents a fundamental requirement for all applications based on twisted light. Hitherto, this has been demonstrated by a variety of methods: exploiting double-slit interference [16], diffraction through single apertures [17–20] or through arrays of pinholes [21], interference with a reference wave [22,23], interferometers [24–26], OAM-dependent Doppler frequency shifts [27–29], phase flattening and spatial mode projection using pitchfork holograms [30–32], q-plates [33,34], spiral phase plates [35] and volume holograms [36], spatial sorting of helical modes by mapping OAM states into

transverse momentum (i.e., propagation direction) [37,38], and quantum weak measurements [39].

General structured fields are, however, not given by individual helical modes, but can always be obtained as suitable superpositions of multiple helical modes. Accordingly, a full experimental characterization of these structured fields can be based on measuring the complex coefficients (amplitude and phase) associated with each mode appearing in the superposition for any given choice of the mode basis. In general, this is not a trivial task, but several methods for the reconstruction of the complex spectrum associated with the OAM degree of freedom have been demonstrated thus far [24,28,29,33,35,36,40,41], possibly including also the radial mode spectrum reconstruction [31,32,37–39,42–44]. It is worth noting that, once these complex coefficients are known, the complete spatial distribution of the electric field can be obtained and important properties such as beam quality factor M^2 , beam width, and wavefront are easily computed at any propagation distance [40,45]. Inspired by previous works [28,29,46,47] introducing Fourier analysis in this context, here we present an approach to the measurement of a light OAM spectrum and, more generally, to spatial mode decomposition of structured light that may prove to be more practical than most alternatives. The OAM complex spectrum information is contained in the intensity pattern resulting from the interference of the light beam with a known reference field (such as a Gaussian beam), and can hence be easily extracted by a suitable

processing of the corresponding images recorded on a camera. First, a Fourier transform with respect to the azimuthal angle leads to determining the complex coefficients associated with each OAM value as a function of the radial coordinate. Numerical integration over the latter then allows one to use this information to determine the OAM power spectrum and, eventually, to decompose each OAM component in terms of radial modes, e.g., LG beams. Remarkably, all of the information associated with the spatial mode decomposition, or with the OAM power spectrum, is contained in a few images whose number does not scale with the dimensionality of the set of detected helical modes. A unique series of data recorded for the characterization of a given field is used for obtaining the decomposition in any basis of spatial modes carrying OAM (LG, HyGG, Bessel), as this choice comes into play only at the stage of image analysis.

2. RESULTS AND DISCUSSION

A. Description of the Technique

In the following, we limit our attention to the case of scalar optics, as extension to the full vector field is simply obtained by applying the same analysis to two orthogonal polarization components. Considering cylindrical coordinates (r, ϕ, z) , the electric field amplitude associated with a monochromatic paraxial beam propagating along the z direction is given by

$$E_s(r, \phi, z, t) = A_s(r, \phi, z)e^{-i(\omega t - kz)}, \quad (1)$$

where ω is the optical frequency and k is the wave number. We refer to E_s as the signal field to distinguish it from the reference beam that will be introduced later on. The information concerning the spatial distribution of the field is contained in the complex envelope $A_s(r, \phi, z)$. Being periodic with respect to the azimuthal coordinate ϕ , such complex function can be expanded into a sum of fundamental helical modes $e^{im\phi}$, carrying $m\hbar$ OAM per photon along the z axis [2],

$$A_s(r, \phi, z) = \sum_{m=K_1}^{K_2} c_m(r, z)e^{im\phi}, \quad (2)$$

where K_1 and K_2 are integer numbers representing the OAM spectrum bounds of the field, respectively (they can also be infinite in the case of unbounded spectra). Coefficients c_m are defined in terms of the angular Fourier transform

$$c_m(r, z) = \frac{1}{2\pi} \int_0^{2\pi} d\phi e^{-im\phi} A_s(r, \phi, z). \quad (3)$$

The probability $P(m)$ that a photon is found in the m -order OAM state is obtained from the coefficients c_m by integrating their squared modulus along the radial coordinate,

$$P(m) = \frac{1}{S} \int_0^\infty dr r |c_m(r, z)|^2, \quad (4)$$

where $S = \sum_m \int_0^\infty dr r |c_m(r, z)|^2$ is the beam power at any transverse plane. The quantity $P(m)$ is also referred to as the OAM power spectrum, or spiral spectrum of the beam, and does not depend on the longitudinal coordinate z because of OAM conservation during propagation. A complete analysis of the field in terms of transverse spatial modes is obtained by replacing $e^{im\phi}$ in Eq. (2) with a complete set of modes having a well-defined radial dependence, e.g., LG modes,

$$A_s(r, \phi, z) = \sum_{p=P_1}^{P_2} \sum_{m=K_1}^{K_2} b_{p,m} \text{LG}_{p,m}(r, \phi, z), \quad (5)$$

where $\text{LG}_{p,m}(r, \phi, z)$ is the complete LG mode of integer indices p and m (with $p \geq 0$) as explicitly defined in Section 4, Methods, and P_1 and P_2 are positive integers defining the bounds for the radial spectrum. The link between coefficients c_m and $b_{p,m}$ is then given by

$$b_{p,m} = \int_0^\infty r dr \text{LG}_{p,m}^*(r, z) c_m(r, z), \quad (6)$$

where we introduced the radial LG amplitudes $\text{LG}_{p,m}(r, z) = \text{LG}_{p,m}(r, \phi, z)e^{-im\phi}$, for which the ϕ dependence is removed.

The procedure we present here allows one to measure the complex quantities $c_m(r)$, or equivalently the coefficients $b_{p,m}$. We achieve this goal by letting the signal optical field interfere with a reference wave $E_{\text{ref}} = A_{\text{ref}}(r, \phi, z)e^{-i(\omega t - kz)}$ having the same polarization, frequency, wavelength, and optical axis of the beam under investigation, and whose spatial distribution is known. The simplest choice for this reference is a Gaussian beam. At any plane transverse to the propagation direction, the intensity pattern I formed by the superposition of signal and reference beams is (we omit the functional dependence on the spatial coordinates)

$$I = I_s + I_{\text{ref}} + \tilde{I}_\alpha. \quad (7)$$

Here I_s and I_{ref} are the intensities corresponding to the sole signal and reference fields, respectively, while the term $\tilde{I}_\alpha = 2 \text{Re}(e^{i\alpha} A_s A_{\text{ref}}^*)$ corresponds to their interference modulation pattern, α being a controllable optical phase between the two. The interference modulation pattern can be experimentally singled out by taking three images, namely I , I_{ref} (blocking the signal beam), and I_s (blocking the reference beam), and then calculating the difference $\tilde{I}_\alpha = I - I_{\text{ref}} - I_s$.

The interference modulation pattern is linked to the OAM mode decomposition by the following expression:

$$\tilde{I}_\alpha = 2 \sum_m |A_{\text{ref}}| |c_m| \cos[m\phi + \alpha + \beta_m], \quad (8)$$

where $\beta_m(r, z) = \text{Arg}[c_m(r, z)] - \text{Arg}[A_{\text{ref}}(r, z)]$. By combining two interference patterns obtained with $\alpha = 0$ and $\alpha = \pi/2$, one then gets

$$\tilde{I}_0 - i\tilde{I}_{\pi/2} = 2 \sum_m |A_{\text{ref}}| |c_m| e^{i(m\phi + \beta_m)}. \quad (9)$$

Finally, Fourier analysis with respect to the azimuthal coordinate allows one to determine the coefficients $c_m(r)$,

$$c_m(r, z) = \frac{1}{4\pi A_{\text{ref}}^*(r, z)} \int_0^{2\pi} d\phi (\tilde{I}_0 - i\tilde{I}_{\pi/2}) e^{-im\phi}, \quad (10)$$

which contains all the information associated with the spatial distribution of the electric field.

The method just described is required for a full modal decomposition and requires taking a total of four images (that is, I with $\alpha = 0$ and $\alpha = \pi/2$, plus I_{ref} and I_s), maintaining also a good interferometric stability between them. However, for applications requiring the measurement of the OAM power spectrum only—that is, ignoring the radial structure of the field, and for which the OAM spectrum is bound from below (that is, there is a minimum OAM value)—there is a simplified procedure that is even easier and more robust (the case for which the spectrum is limited from

above can be treated equivalently). In the case of beams containing helical modes with both positive and negative charges [$K_1 < 0$ and $K_2 > 0$ in Eq. (2)], this usually requires having the signal beam first pass through a spiral optical phase element, described by the transfer factor $e^{iM\phi}$ (this can be achieved with a q -plate or a spiral phase plate with the appropriate topological charge). If $M > |K_1|$, the spiral spectrum of the beam after this optical component will contain only modes associated with positive OAM values. If K_1 and K_2 have the same sign, this preliminary procedure can be skipped. Then, one can extract the associated probabilities $P(m)$ by Fourier analysis of \tilde{I}_0 only [see Eq. (8)], with no need of also measuring $\tilde{I}_{\pi/2}$, thus reducing the number of required images to three and simplifying the setup. We discuss this in detail in the final part of the paper.

B. Experimental Results

We demonstrate the validity of our technique by determining the OAM spectrum and the radial profile of the associated helical modes for a set of structured light fields. The setup is shown in Fig. 1 and described in detail in the figure caption. Here, structured light containing multiple OAM components is generated by means of q -plates, consisting essentially of a thin layer of liquid crystals whose local optic axes are arranged in a singular pattern, characterized by a topological charge q [48,49]. The way such a

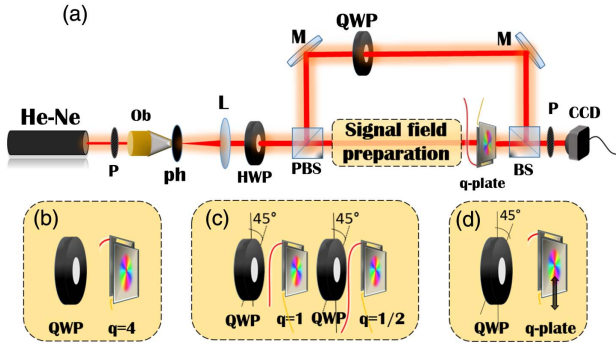


Fig. 1. Sketch of the experimental apparatus. (a) A He–Ne laser beam passes through a polarizer (P) and is spatially cleaned and collimated by means of an objective (Ob), a pinhole (ph) and a lens (L). A half-wave plate (HWP) and a polarizing beam splitter (PBS) are used in order to split the beam into the signal and reference arms, whose relative intensities can be controlled by HWP rotation. Fields resulting from a complex superposition of multiple helical modes were obtained by using q -plates and quarter-wave plates (QWPs), as shown in panels (b) and (c). After preparing the signal field, we place a further sequence of a QWP and a q -plate in case we need to shift the entire OAM spectrum. The reference field is a $TEM_{0,0}$ Gaussian mode. In the upper arm of the interferometer, by orienting the QWP at 0 or 90° with respect to the beam polarization we can introduce a $\alpha = 0$ or $\pi/2$ phase delay between the signal and the reference field, respectively. The two beams are superimposed at the exit of a beam splitter (BS) and filtered through a polarizer, so that they share the same polarization state. The emerging intensity pattern is recorded on a CCD camera (with resolution 576×668). (b) A QWP oriented at 45° or 0, followed by q -plate with $q = 4$ and $\delta = \pi$ or $\delta = \pi/2$, is used for the generation of a light beam containing a single mode ($m = 8$) or three modes ($m = -8, 0, 8$), respectively. (c) two q -plates with $q = 1$ and $q = 1/2$ are aligned to generate spectra with $m \in [-3, 3]$. (d) A set of more complex distributions was obtained by displacing laterally the centre of a q -plate ($q = 1$ and $\delta = \pi$) with respect to the axis of the impinging Gaussian beam.

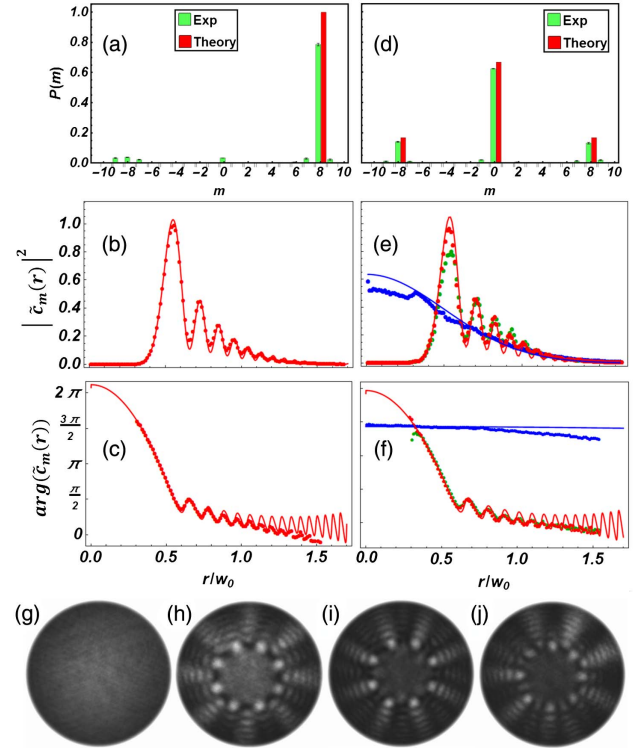


Fig. 2. Experimental reconstruction of light OAM spectrum. We report the experimental characterization of optical fields containing one (a–b–c) and three (d–e–f) helical modes, generated using a q -plate with $q = 4$ and $\delta = \pi$ or $\pi/2$, respectively. In panels (g)–(j) we report the experimental intensity patterns I_{ref} , I_s , I_0 and $I_{\pi/2}$, respectively, obtained when investigating the field generated by the q -plate with $\delta = \pi/2$. Panels (a) and (d) show the OAM distributions in the two cases. Error bars are calculated as three times the standard error. Panels (b), (c) and (e), (f) show the measured amplitude and phase profiles of the non-vanishing helical modes that are present in the beam, where blue, red and green colored points are associated with modes with $m = 0, 8, -8$, respectively. These results are compared with theoretical simulations, represented as continuous curves with the same color scheme adopted for the experimental results. For each value of m , we plot normalized coefficients $\tilde{c}_m = c_m/S_m$, where S_m is the total power associated with the helical mode. As expected from theory, a fraction of the beam is left in the fundamental Gaussian state, while an equal amount of light is converted into helical modes with $m = \pm 8$, both having the radial profile of a HyGG $_{-8,8}$ mode. Simulated profiles of Gaussian and HyGG modes correspond to $w_0 = 1.45$ mm and $z = 30$ cm, the latter being the distance between the q -plate and the camera. Error bars are smaller than experimental points.

device modifies the spatial properties of a light beam is described in detail in Section 4, Methods.

In Figs. 2(a)–2(c) and 2(d)–2(f), we report the results of our first experiment, consisting of the measurement of both amplitude and phase of coefficients $c_m(r)$ of optical fields having one ($m = 8$) and three ($m = \{-8, 0, 8\}$) different helical modes, respectively, accompanied by the associated OAM power spectrum [see Eq. (4)]. We generate such structured light by shining a q -plate with $q = 4$ with a left-circularly (horizontally) polarized Gaussian beam and setting the plate optical retardation δ to the value π ($\pi/2$), respectively (see Section 4, Methods). Our data nicely follows the results from our simulations, with some minor deviations that are due to imperfections in the preparation of the

structured fields. In particular, in panel a, the small peaks centered around $m = -8$ are related to the possible ellipticity of the polarization of the Gaussian beam impinging on the q -plate, while a small contribution at $m = 0$ corresponds to the tiny fraction of the input beam that has not been converted by the q -plate. In panels b and e, the radial profiles used for our simulations are those corresponding to the Hypergeometric-Gaussian modes [3], the helical modes that are expected to describe the optical field at the exit of the q -plate [50] (see Section 4, Methods, for details). Error bars shown in our plots are those associated with the variability in selecting the correct center $r = 0$ in the experimental images, which is identified as one of the main sources of uncertainty in the spectral results. They are estimated as three times the standard deviation of the data computed after repeating our analysis with the coordinate origin set in one of 25 pixels that surround our optimal choice. Other possible systematic errors, such as, for example, slight misalignments between the signal and reference fields, are not considered here.

Data reported in Fig. 2 prove our ability to measure the complete radial distribution of the field associated with individual helical modes in a superposition. For each of these, we can use our results to obtain a decomposition in terms of a complete set of modes. For a demonstration of this concept, we consider the field obtained when a left-circularly polarized beam passes through a q -plate with $q = 4$ and $\delta = \pi$. The latter contains only a mode with $m = 8$, as shown in Figs. 2(a)–2(c). By evaluating the integrals reported in Eq. (6), we determine the coefficients $b_{p,8}$ of a LG decomposition. For our analysis, we use LG beams with an optimal waist parameter \tilde{w}_0 (different from the one of the impinging Gaussian beam), defined so that the probability of the lowest radial index $p = 0$ is maximal [51]. In Fig. 3, we plot the squared modulus and phase of the coefficients $b_{p,8}$ determined experimentally, matching nicely the results obtained from numerical simulations.

C. Shifting the OAM Power Spectrum

As mentioned above, shifting the OAM spectrum of the signal field may be used to simplify its measurement when reconstructing the radial profile is not needed. In our case, we let the signal field pass through a q -plate with $q = M/2$ and $\delta = \pi$, after

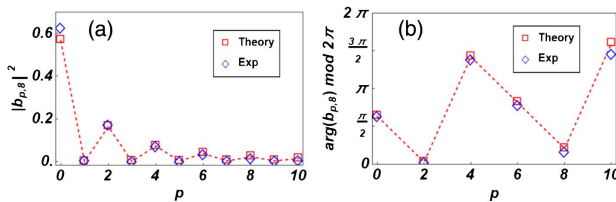


Fig. 3. Complete spatial mode decomposition in terms of LG beams. We consider the light beam emerging from a q -plate with ($q = 4$, $\delta = \pi$), described by a HyGG $_{-8,8}$ mode [50]. We evaluate the overlap integral between the radial envelope $c_8(r)$ measured in our experiment at $z = 30$ cm and LG $_{p,8}$ modes at the same value of z and characterized by the optimal beam waist $\tilde{w}_0 = w_0/3$ [51], where w_0 is the input beam waist. In panels (a) and (b) we plot the squared modulus and the phase of the resulting coefficients (blue markers), respectively, showing a good agreement with the values obtained from numerical simulations (red markers). The phases of $b_{p,8}$ with p equal to odd integers are absent in the plot since the corresponding amplitudes are consistent with zero, that is smaller than the associated statistical uncertainties.

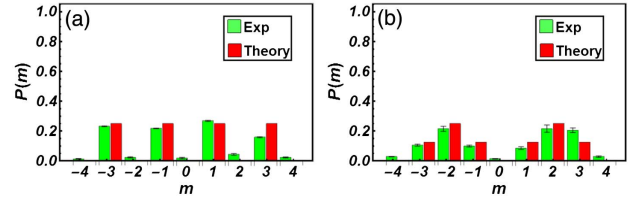


Fig. 4. Measure of shifted OAM power spectrum. OAM probability distributions are measured for two different optical fields, obtained when shining a sequence of two q -plates with $q_1 = 1$ and $q_2 = 1/2$ with horizontally polarized light. A further q -plate with $q = 4$ shifts the final spectrum by $M = 8$ units. (a) OAM spectrum for the case $\delta_1 = \pi$ and $\delta_2 = \pi$. (b) The same data are reported for a different field, obtained when $\delta_1 = \pi$ and $\delta_2 = \pi/2$. Error bars represent the standard error multiplied by three.

preparing it in a state of left-circular polarization. If M is large enough, i.e., higher than K_1 [see Eq. (2)], we have that $c(m) \neq 0$ only if $m > 0$. This allows, in turn, using Eq. (8) to determine the OAM spectrum, instead of Eq. (9), which requires the measurement of $I_{\pi/2}$ also. At the same time, this approach is less sensitive to possible noise related to beam imperfections or slight misalignments, typically associated with small spatial frequencies, that affect the lowest-order helical modes, as reported also in Refs. [28,29]. Let us note that once the beam passes through an optical element adding the azimuthal phase $e^{iM\phi}$, thanks to the conservation of OAM during free propagation, the associated power OAM spectrum is only shifted by M units, that is, $P(m) \rightarrow P(m + M)$. The radial distribution of individual helical modes, on the other hand, is altered during propagation, that is, $c_m(r, z) \rightarrow c_{m+M}(r, z)$. For this reason, this alternative procedure proves convenient only when determining the OAM probability distribution, but cannot be applied to the reconstruction of the full modal decomposition. In Fig. 4, we report the measured power spectrum of different fields containing helical modes with $m \in [-3, 3]$ (see Section 4 (Methods) and the figure caption for further details on the generation of such complex fields), as determined by shifting the OAM spectrum by $M = 8$ by means of a q -plate with $q = 4$ and $\delta = \pi$.

D. OAM Spectra for Displaced q -Plates

As a final test, we used our technique for characterizing more complex optical fields, such as those emerging from a q -plate whose central singularity is displaced with respect to the input Gaussian beam axis [Fig. 1(c)]. In Fig. 5, we report the OAM probability distributions obtained when translating a q -plate ($q = 1$, $\delta = \pi$) in a direction that is parallel to the optical table, with steps of $\Delta x = 0.125$ mm. Our data are in excellent agreement with results obtained from numerical simulations. In the same figure, we show part of the associated total intensity patterns I_0 [see Eq. (7)] recorded on the camera. In addition, for each configuration, we show in Fig. 5 that the first- and second-order moments of the probability distributions are characterized by Gaussian profiles $\langle m \rangle = 2q \exp(-2x_0^2/w_0^2)$ and $\langle m^2 \rangle = (2q)^2 \exp(-2x_0^2/w_0^2)$ [52]. Fitting our data so that they follow the expected Gaussian distributions (red curves), we obtain $w_0^{\text{fit}} = 1.36 \pm 0.04$ mm from $\langle m \rangle$ (panel g), and $w_0^{\text{fit}} = 1.39 \pm 0.06$ mm from $\langle m^2 \rangle$ (panel h), which are close to the expected value $w_0 = 1.45 \pm 0.18$ mm.

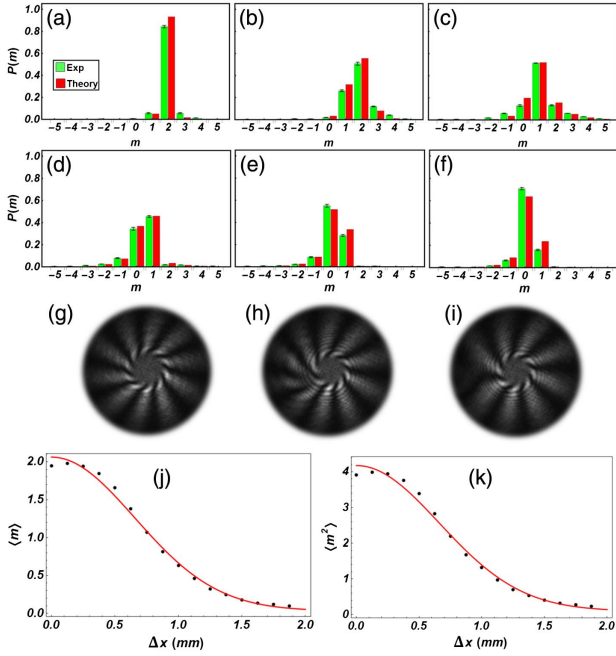


Fig. 5. OAM spectrum for a shifted q -plate. We measure the OAM power spectrum at the exit of a q -plate ($q = 1$, $\delta = \pi$) shifted with respect to the axis of the impinging Gaussian beam, which is left-circularly polarized. The overall spectrum is shifted by $M = 8$ units since we are using a further q -plate with $q = 4$ and $\delta = \pi$. However, we plot the original OAM distribution associated with the signal field. (a)–(f) Experimental (green) and simulated (red) OAM power spectra when the lateral shift is equal to $a\Delta x$, with $a = 1, 3, 6, 9, 12, 15$ and $\Delta x = 0.125$ mm, respectively. Error bars represent the standard error multiplied by three. (g)–(i) Examples of the experimental intensity pattern I_0 used for determining the power spectra reported in panels (a), (c), (e). The number of azimuthal fringes reveals that the OAM spectrum has been shifted. (j) and (k) First and second moment ($\langle m \rangle$ and $\langle m^2 \rangle$) measured as a function of the lateral displacement. Error bars are not visible because smaller than the experimental points.

E. Range of Detectable Helical Modes

Finite size of the detector area and the camera resolution impose natural limitations to our approach that cannot be used to characterize helical modes with arbitrary values of m and radial profiles. Starting from these considerations, in Section 4, Methods, we describe how to evaluate the bandwidth of detectable LG modes in terms of sensor area and resolution, and provide an explicit example for our specific configuration (associated data are reported in Fig. 6).

3. CONCLUSIONS

In this study we introduced a new technique for measuring the OAM spectrum of a laser beam accompanied by its complete spatial mode decomposition in terms of an arbitrary set of modes that carry a definite amount of OAM, such as LG beams or others. Based on the azimuthal Fourier analysis of the interference pattern formed by the signal and the reference field, relying on only a few measurements, this approach allows one to readily extract the information contained in both the radial and azimuthal degrees of freedom of a structured light beam. Standard interferometric techniques, as reported for instance in Refs. [53,54], are

commonly used for the measurement of the phase profile of optical waves, allowing for the measurement of the complex spatial envelope \mathcal{A}_i of the field [see Eq. (1)]. However, using this information to obtain the decomposition in terms of a complete set of helical modes [using Eqs. (3) and (6)], and, in turn, the OAM power spectrum, has not been thoroughly explored before. Furthermore, when interested in the spiral spectrum only, we demonstrated that it is actually possible to retrieve the OAM distribution without measuring the complete field, making use of a reduced number of measurements.

In our approach, the most general method requires taking four images, including the intensity patterns of the signal beam, the reference beam, and two interference patterns between them. Information on the modal decomposition of the signal field is then retrieved using a simple dedicated software. Since the spatial mode decomposition is obtained during this post-processing procedure, the same set of images can be used to decompose a beam in different sets of spatial modes. As demonstrated here, the experimental implementation of our approach requires a simple interferometric scheme and minimal equipment. Hence, it may be readily extended to current experiments dealing with the characterization of spatial properties and OAM decomposition of structured light.

4. METHODS

A. Spatial Modes Carrying OAM

Using adimensional cylindrical coordinates $\rho = r/w_0$ and $\zeta = z/z_R$, where w_0 is the waist radius of the Gaussian envelope and z_R the Rayleigh range, respectively, Laguerre–Gaussian $\text{LG}_{p,m}$ modes have the well-known expression

$$\begin{aligned} \text{LG}_{p,m}(\rho, \zeta, \phi) = & \sqrt{\frac{2^{|m|+1} p!}{\pi(p+|m|)!(1+\zeta^2)}} \left(\frac{\rho}{\sqrt{1+\zeta^2}} \right)^{|m|} \\ & \times e^{-\frac{\rho^2}{1+\zeta^2}} L_p^{|m|}(2\rho^2/(1+\zeta^2)) \\ & \times e^{i\frac{p^2}{\zeta+1/\zeta}} e^{im\phi - i(2p+|m|+1)\arctan(\zeta)}, \end{aligned} \quad (11)$$

where $L_p^{|m|}(x)$ is the generalized Laguerre polynomial, p is a positive integer, and m is the azimuthal index associated with the OAM.

When a Gaussian beam passes through an optical element that impinges on it a phase factor $e^{im\phi}$, the outgoing field is described by a Hypergeometric-Gaussian mode $\text{HyGG}_{p,m}$ [3,50] with $p = -|m|$,

$$\begin{aligned} \text{HyGG}_{p,m}(\rho, \zeta, \phi) = & \sqrt{\frac{2^{1+|m|+p}}{\pi\Gamma(1+|m|+p)}} \frac{\Gamma(1+|m|+p/2)}{\Gamma(1+|m|)} \\ & \times i^{|m|+1} \zeta^{p/2} (\zeta+i)^{-(1+|m|+p/2)} \\ & \times \rho^{|m|} e^{-i\rho^2/(\zeta+i)+im\phi} \\ & \times {}_1F_1(-p/2; |m|+1; \rho^2/(\zeta(\zeta+i))), \end{aligned} \quad (12)$$

where $\Gamma(z)$ is the Euler Gamma function and ${}_1F_1(a; b; z)$ is the confluent Hypergeometric function.

B. Generating Structured Light Using q -Plates

A q -plate is formed by a thin layer of liquid crystals; the angle α describing the orientation of the optic axis of such molecules is a

linear function of the azimuthal angle, that is, $\alpha(\phi) = \alpha_0 + q\phi$ (q is the topological charge, given by integer or semi-integer numbers). In our experiments, we set $\alpha_0 = 0$. In this case, the action of the q -plate is described by the following Jones matrix (in the basis of circular polarizations):

$$\hat{Q}(\delta) = \cos\left(\frac{\delta}{2}\right) \begin{pmatrix} 1 & 0 \\ 0 & 1 \end{pmatrix} + i \sin\left(\frac{\delta}{2}\right) \begin{pmatrix} 0 & e^{-im\phi} \\ e^{im\phi} & 0 \end{pmatrix}, \quad (13)$$

where $m = 2q$ and δ is the plate optical retardation, controllable by applying an external electric field [55]. It is worth noting that the second term of Eq. (13) introduces the azimuthal dependence associated with the OAM degree of freedom. When a left- or right-circularly polarized Gaussian beam passes through a q -plate with $\delta = \pi$, positioned at the waist of the beam, the output beam is given by $\text{HyGG}_{-|m|, \pm m}$ respectively [50]. In our experiment, we generated superpositions of several OAM modes using single or cascaded q -plates, characterized by specific values of q and δ that are reported in the figure captions.

C. Limitations on the Set of Detectable Spatial Modes

We briefly discussed in the main text that the finite size of the detector area and the finite dimension of sensor pixels impose certain restrictions on the features of the helical modes that can be resolved and correctly detected in our setup. Let us consider the simple case wherein we want to decompose the signal field in terms of $\text{LG}_{p,m}$ modes and we want to evaluate the p , m -bandwidth of detectable modes. We consider only the case $m > 0$, since only the absolute value $|m|$ is relevant to our discussion. Consider a camera with $N \times N$ pixels, with pixel dimensions $d \times d$ (in our setup $N = 576$ and $d = 9 \mu\text{m}$). We define the following quantities:

$$r_{\max} = d * N/2, \quad (14)$$

$$r_{\min} = md/\pi, \quad (15)$$

$$r_1 = w(z) \left\{ \frac{2p + m - 2 - [1 + 4(p-1)(p+m-1)]^{1/2}}{2} \right\}^{1/2}, \quad (16)$$

$$r_p = w(z) \left\{ \frac{2p + m - 2 + [1 + 4(p-1)(p+m-1)]^{1/2}}{2} \right\}^{1/2}, \quad (17)$$

$$\tilde{r}_p = w(z) \{2p + m + 1\}^{1/2}. \quad (18)$$

Here r_{\max} is the maximum radius available on the sensor; r_{\min} is the minimum radial distance where azimuthal oscillation associated with the OAM content of the $\text{LG}_{p,m}$ mode can be detected, before facing aliasing issues; r_1 is a lower bound for the first root of the Laguerre polynomials contained in the expression of LG modes; similarly, r_p is the upper bound for the p -th root, while \tilde{r}_p , with $r_p < \tilde{r}_p$, delimits the oscillatory region of the Laguerre polynomials [56,57]. Interestingly, the spatial region $r_1 < r < \tilde{r}_p$ well approximates the area containing all the power associated with the mode. At the same time, the quantity $\Lambda = (r_p - r_1)/p$ well describes the average distance between consecutive nodes of the LG mode, defining the periodicity of their radial oscillations. A given $\text{LG}_{p,m}$ mode is then “detectable” (or properly “resolvable”) if all the following conditions are satisfied:

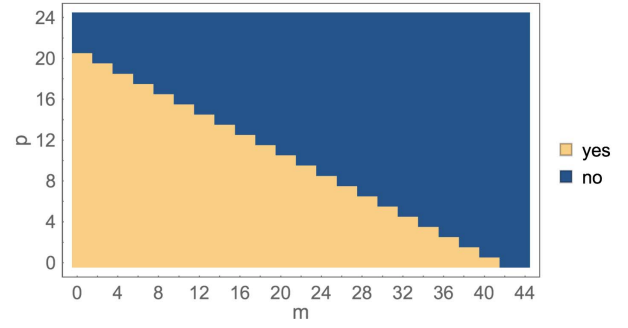


Fig. 6. Detectable LG modes. Different colors, as reported in the legend, indicate whether a specific $\text{LG}_{p,m}$, in a transverse plane $z = 30$ cm and with a beam waist $w_0 = 0.16$ mm [$w(z = 30 \text{ cm}) \rightarrow 0.4$ mm] can be resolved in our setup. These parameters correspond to the ones used for the complete spatial decomposition of the HyGG beam generated by a q -plate ($q = 4$, $\delta = \pi$) in terms of LG beams.

$$\begin{cases} r_{\min} < r_1 & \text{(i)} \\ r_p < r_{\max} & \text{(ii)} \\ \Lambda > 2d & \text{(iii)} \end{cases}. \quad (19)$$

Indeed, we are requiring (i) that the field is vanishing below the azimuthal aliasing threshold given by r_{\min} ; (ii) that all the power associated with the mode is contained in the sensor area, and (iii) that the field radial oscillations have a spatial period such that at least two pixels are contained in a single period, respectively (radial aliasing limit). It is easy to check that in our configuration, where the beam waist is $w(z) = 0.4$ mm, conditions (i) and (iii) are always satisfied for the values of $\{p, m\}$ that are solutions of (ii), i.e., the limiting factor is only the dimension of the sensor area. By solving such inequality, we get the relation

$$p < \left(\frac{N^2 d^2}{4w^2(z)} - m - 1 \right) / 2. \quad (20)$$

In Fig. 6 we plot a colormap for a rapid visualization of detectable modes. If we apply this analysis to the case of Fig. 3, in which a beam with $m = 8$ is studied, we obtain that only radial modes with $p < 16$ can be detected. In general, for smaller values of $w(z)$, the determination of a detectable LG mode is more complex and requires the complete resolution of the system of inequalities system given in (19).

Funding. H2020 European Research Council (ERC) (694683 (PHOSPhOR)).

REFERENCES

1. L. Allen, M. W. Beijersbergen, R. J. C. Spreeuw, and J. P. Woerdman, “Orbital angular momentum of light and the transformation of Laguerre-Gaussian laser modes,” *Phys. Rev. A* **45**, 8185–8189 (1992).
2. A. M. Yao and M. J. Padgett, “Orbital angular momentum: origins, behavior and applications,” *Adv. Opt. Photon.* **3**, 161–204 (2011).
3. E. Karimi, G. Zito, B. Piccirillo, L. Marrucci, and E. Santamato, “Hypergeometric-Gaussian modes,” *Opt. Lett.* **32**, 3053–3055 (2007).
4. K. Y. Bliokh, F. J. Rodríguez-Fortuño, F. Nori, and A. V. Zayats, “Spin-orbit interactions of light,” *Nat. Photonics* **9**, 796–808 (2015).
5. F. Cardano and L. Marrucci, “Spin-orbit photonics,” *Nat. Photonics* **9**, 776–778 (2015).
6. H. Rubinsztein-Dunlop, A. Forbes, M. V. Berry, M. R. Dennis, D. L. Andrews, M. Mansuripur, C. Denz, C. Alpmann, P. Banzer, T. Bauer,

- E. Karimi, L. Marrucci, M. Padgett, M. Ritsch-Martens, N. M. Litchinitser, N. P. Bigelow, C. Rosales-Guzmán, A. Belmonte, J. P. Torres, T. W. Neely, M. Baker, R. Gordon, A. B. Stilgoe, J. Romero, A. G. White, R. Fickler, A. E. Willner, G. Xie, B. McMorran, and A. M. Weiner, "Roadmap on structured light," *J. Opt.* **19**, 013001 (2017).
7. G. Vallone, V. D'Ambrosio, A. Sponselli, S. Slussarenko, L. Marrucci, F. Sciarrino, and P. Villoresi, "Free-space quantum key distribution by rotation-invariant twisted photons," *Phys. Rev. Lett.* **113**, 060503 (2014).
 8. A. E. Willner, H. Huang, Y. Yan, Y. Ren, N. Ahmed, G. Xie, C. Bao, L. Li, Y. Cao, Z. Zhao, J. Wang, M. P. J. Lavery, M. Tur, S. Ramachandran, A. F. Molisch, N. Ashrafi, and S. Ashrafi, "Optical communications using orbital angular momentum beams," *Adv. Opt. Photon.* **7**, 66–106 (2015).
 9. M. Mirhosseini, O. S. Magaña-Loaiza, M. N. O'sullivan, B. Rodenburg, M. Malik, M. P. J. Lavery, M. J. Padgett, D. J. Gauthier, and R. W. Boyd, "High-dimensional quantum cryptography with twisted light," *New J. Phys.* **17**, 033033 (2015).
 10. F. Bouchard, R. Fickler, R. W. Boyd, and E. Karimi, "High-dimensional quantum cloning and applications to quantum hacking," *Sci. Adv.* **3**, e1601915 (2017).
 11. X.-L. Wang, X.-D. Cai, Z.-E. Su, M.-C. Chen, D. Wu, L. Li, N.-L. Liu, C.-Y. Lu, and J.-W. Pan, "Quantum teleportation of multiple degrees of freedom of a single photon," *Nature* **518**, 516–519 (2015).
 12. M. Malik, M. Erhard, M. Huber, M. Krenn, R. Fickler, and A. Zeilinger, "Multi-photon entanglement in high dimensions," *Nat. Photonics* **10**, 248–252 (2016).
 13. B. Hiesmayr, M. de Dood, and W. Löffler, "Observation of four-photon orbital angular momentum entanglement," *Phys. Rev. Lett.* **116**, 073601 (2016).
 14. F. Cardano, M. Maffei, F. Massa, B. Piccirillo, C. de Lisio, G. De Filippis, V. Cataudella, E. Santamato, and L. Marrucci, "Statistical moments of quantum-walk dynamics reveal topological quantum transitions," *Nat. Commun.* **7**, 11439 (2016).
 15. F. Cardano, A. D'Errico, A. Dauphin, M. Maffei, B. Piccirillo, C. de Lisio, G. De Filippis, V. Cataudella, E. Santamato, L. Marrucci, M. Lewenstein, and P. Massignan, "Detection of Zak phases and topological invariants in a chiral quantum walk of twisted photons," *Nat. Commun.* **8**, 15516 (2017).
 16. H. I. Sztul and R. R. Alfano, "Double-slit interference with Laguerre–Gaussian beams," *Opt. Lett.* **31**, 999–1001 (2006).
 17. J. M. Hickmann, E. J. S. Fonseca, W. C. Soares, and S. Chávez-Cerda, "Unveiling a truncated optical lattice associated with a triangular aperture using light's orbital angular momentum," *Phys. Rev. Lett.* **105**, 053904 (2010).
 18. Q. S. Ferreira, A. J. Jesus-Silva, E. J. S. Fonseca, and J. M. Hickmann, "Fraunhofer diffraction of light with orbital angular momentum by a slit," *Opt. Lett.* **36**, 3106–3108 (2011).
 19. A. Mourka, J. Baumgartl, C. Shanor, K. Dholakia, and E. M. Wright, "Visualization of the birth of an optical vortex using diffraction from a triangular aperture," *Opt. Express* **19**, 5760–5771 (2011).
 20. M. Mazilu, A. Mourka, T. Vetteng, E. M. Wright, and K. Dholakia, "Simultaneous determination of the constituent azimuthal and radial mode indices for light fields possessing orbital angular momentum," *Appl. Phys. Lett.* **100**, 231115 (2012).
 21. G. C. G. Berkhout and M. W. Beijersbergen, "Method for probing the orbital angular momentum of optical vortices in electromagnetic waves from astronomical objects," *Phys. Rev. Lett.* **101**, 100801 (2008).
 22. M. Harris, C. A. Hill, P. R. Tapster, and J. M. Vaughan, "Laser modes with helical wave fronts," *Phys. Rev. A* **49**, 3119–3122 (1994).
 23. M. Padgett, J. Arit, N. Simpson, and L. Allen, "An experiment to observe the intensity and phase structure of Laguerre–Gaussian laser modes," *Am. J. Phys.* **64**, 77–82 (1996).
 24. J. Leach, M. J. Padgett, S. M. Barnett, S. Franke-Arnold, and J. Courtial, "Measuring the orbital angular momentum of a single photon," *Phys. Rev. Lett.* **88**, 257901 (2002).
 25. S. Slussarenko, V. D'Ambrosio, B. Piccirillo, L. Marrucci, and E. Santamato, "The Polarizing Sagnac Interferometer: a tool for light orbital angular momentum sorting and spin-orbit photon processing," *Opt. Express* **18**, 27205–27216 (2010).
 26. M. P. J. Lavery, A. Dudley, A. Forbes, J. Courtial, and M. J. Padgett, "Robust interferometer for the routing of light beams carrying orbital angular momentum," *New J. Phys.* **13**, 093014 (2011).
 27. J. Courtial, D. A. Robertson, K. Dholakia, L. Allen, and M. J. Padgett, "Rotational frequency shift of a light beam," *Phys. Rev. Lett.* **81**, 4828–4830 (1998).
 28. M. V. Vasnetsov, J. P. Torres, D. V. Petrov, and L. Torner, "Observation of the orbital angular momentum spectrum of a light beam," *Opt. Lett.* **28**, 2285–2287 (2003).
 29. H.-L. Zhou, D.-Z. Fu, J.-J. Dong, P. Zhang, D.-X. Chen, X.-L. Cai, F.-L. Li, and X.-L. Zhang, "Orbital angular momentum complex spectrum analyzer for vortex light based on the rotational Doppler effect," *Light Sci. Appl.* **6**, e16251 (2016).
 30. A. Mair, A. Vaziri, G. Weihs, and A. Zeilinger, "Entanglement of the orbital angular momentum states of photons," *Nature* **412**, 313–316 (2001).
 31. T. Kaiser, D. Flamm, S. Schröter, and M. Duparré, "Complete modal decomposition for optical fibers using CGH-based correlation filters," *Opt. Express* **17**, 9347–9356 (2009).
 32. C. Schulze, A. Dudley, D. Flamm, M. Duparré, and A. Forbes, "Measurement of the orbital angular momentum density of light by modal decomposition," *New J. Phys.* **15**, 073025 (2013).
 33. E. Karimi, B. Piccirillo, E. Nagali, L. Marrucci, and E. Santamato, "Efficient generation and sorting of orbital angular momentum eigenmodes of light by thermally tuned q-plates," *Appl. Phys. Lett.* **94**, 231124 (2009).
 34. E. Karimi, L. Marrucci, C. de Lisio, and E. Santamato, "Time-division multiplexing of the orbital angular momentum of light," *Opt. Lett.* **37**, 127–129 (2012).
 35. P. Bierdz, M. Kwon, C. Roncaioli, and H. Deng, "High fidelity detection of the orbital angular momentum of light by time mapping," *New J. Phys.* **15**, 113062 (2013).
 36. M. T. Gruneisen, R. C. Dymale, K. E. Stoltenberg, and N. Steinhoff, "Optical vortex discrimination with a transmission volume hologram," *New J. Phys.* **13**, 083030 (2011).
 37. G. C. G. Berkhout, M. P. J. Lavery, J. Courtial, M. W. Beijersbergen, and M. J. Padgett, "Efficient sorting of orbital angular momentum states of light," *Phys. Rev. Lett.* **105**, 153601 (2010).
 38. M. Mirhosseini, M. Malik, Z. Shi, and R. W. Boyd, "Efficient separation of the orbital angular momentum eigenstates of light," *Nat. Commun.* **4**, 1–6 (2013).
 39. M. Malik, M. Mirhosseini, M. P. J. Lavery, J. Leach, M. J. Padgett, and R. W. Boyd, "Direct measurement of a 27-dimensional orbital-angular-momentum state vector," *Nat. Commun.* **5**, 3115 (2014).
 40. A. Forbes, A. Dudley, and M. McLaren, "Creation and detection of optical modes with spatial light modulators," *Adv. Opt. Photon.* **8**, 200–227 (2016).
 41. P. Zhao, S. Li, X. Feng, K. Cui, F. Liu, W. Zhang, and Y. Huang, "Measuring the complex orbital angular momentum spectrum of light with a mode-matching method," *Opt. Lett.* **42**, 1080–1083 (2017).
 42. G. C. G. Berkhout, M. P. J. Lavery, M. J. Padgett, and M. W. Beijersbergen, "Measuring orbital angular momentum superpositions of light by mode transformation," *Opt. Lett.* **36**, 1863–1865 (2011).
 43. M. Mirhosseini, O. S. Magaña-Loaiza, S. Omar, C. Chen, S. M. Hashemi Rafsanjani, and R. W. Boyd, "Wigner distribution of twisted photons," *Phys. Rev. Lett.* **116**, 1–6 (2016).
 44. R. Fickler, M. Ginoya, and R. W. Boyd, "Custom-tailored spatial mode sorting by controlled random scattering," *Phys. Rev. B* **95**, 161108 (2017).
 45. C. Schulze, S. Ngcobo, M. Duparré, and A. Forbes, "Modal decomposition without a priori scale information," *Opt. Express* **20**, 27866–27873 (2012).
 46. A. F. Abouraddy, T. M. Yarnall, and B. E. A. Saleh, "Angular and radial mode analyzer for optical beams," *Opt. Lett.* **36**, 4683–4685 (2011).
 47. V. Grillo, G. C. Gazzadi, E. Mafakheri, S. Frabboni, E. Karimi, and R. W. Boyd, "Holographic generation of highly twisted electron beams," *Phys. Rev. Lett.* **114**, 034801 (2015).
 48. L. Marrucci, C. Manzo, and D. Paparo, "Optical spin-to-orbital angular momentum conversion in inhomogeneous anisotropic media," *Phys. Rev. Lett.* **96**, 163905 (2006).
 49. L. Marrucci, E. Karimi, S. Slussarenko, B. Piccirillo, E. Santamato, E. Nagali, and F. Sciarrino, "Spin-to-orbital conversion of the angular momentum of light and its classical and quantum applications," *J. Opt.* **13**, 064001 (2011).

50. E. Karimi, B. Piccirillo, L. Marrucci, and E. Santamato, "Light propagation in a birefringent plate with topological charge," *Opt. Lett.* **34**, 1225–1227 (2009).
51. G. Vallone, "Role of beam waist in Laguerre–Gauss expansion of vortex beams," *Opt. Lett.* **42**, 1097–1100 (2017).
52. B. Piccirillo, S. Slussarenko, L. Marrucci, and E. Santamato, "Directly measuring mean and variance of infinite-spectrum observables such as the photon orbital angular momentum," *Nat. Commun.* **6**, 8606 (2015).
53. M. Takeda, H. Ina, and S. Kobayashi, "Fourier-transform method of fringe-pattern analysis for computer-based topography and interferometry," *J. Opt. Soc. Am.* **72**, 156–160 (1982).
54. I. Yamaguchi and T. Zhang, "Phase-shifting digital holography," *Opt. Lett.* **22**, 1268–1270 (1997).
55. B. Piccirillo, V. D'Ambrosio, S. Slussarenko, L. Marrucci, and E. Santamato, "Photon spin-to-orbital angular momentum conversion via an electrically tunable q-plate," *Appl. Phys. Lett.* **97**, 241104 (2010).
56. M. E. H. Ismail and X. Li, "Bound on the extreme zeros of orthogonal polynomials," *Proc. Am. Math. Soc.* **115**, 131–140 (1992).
57. L. Gatteschi, "Asymptotics and bounds for the zeros of Laguerre polynomials: a survey," *J. Comput. Appl. Math.* **144**, 7–27 (2002).